



ELSEVIER

Contents lists available at ScienceDirect

## Advanced Powder Technology

journal homepage: [www.elsevier.com/locate/apt](http://www.elsevier.com/locate/apt)

Translated Paper: SPTJ Best Paper Award 2020

Real-scale DEM simulations on the fault evolution process observed in sandbox experiments <sup>☆,☆☆</sup>Daisuke Nishiura <sup>a,\*</sup>, Mikito Furuichi <sup>a</sup>, Hide Sakaguchi <sup>b</sup><sup>a</sup> Center for Mathematical Science and Advanced Technology, Japan Agency for Marine-Earth Science and Technology, 3173-25 Showa-machi, Kanazawa-ku, Yokohama 236-0001, Japan<sup>b</sup> Ocean Policy Research Institute, The Sasakawa Peace Foundation, 1-15-16 Toranomon, Minato-ku, Tokyo 105-8524, Japan

## ARTICLE INFO

## Article history:

Received 17 August 2021

Accepted 2 September 2021

Available online 17 September 2021

## Keywords:

Simulation

Fault slip

Accretionary prism

High performance computing

Discrete element method

## ABSTRACT

The study of fault structures and stress states in accretionary prisms is important to elucidate the building and releasing of seismic energy as they control the generation of great earthquakes and tsunami. In this paper, we present the evolution process of three-dimensional fault structures performed in sandbox simulations using a discrete element method (DEM). To realize a real-scale sandbox simulation, we developed state-of-the-art techniques in high performance parallel computing for the DEM and performed the world's largest DEM simulation using up to 1.9 billion particles with a similar grain size as real sand to identify the three-dimensional fault structure. The DEM simulations reproduced the undulation of fault structures, similar to those commonly found in nature. In addition, the characteristic grain motion was observed near the frontal fault before the commencement of the uplift event of the sand bed, which could be a precursor of tectonic events behind accretionary prism formation.

© 2021 The Society of Powder Technology Japan. Published by Elsevier B.V. and The Society of Powder Technology Japan. This is an open access article under the CC BY-NC-ND license (<http://creativecommons.org/licenses/by-nc-nd/4.0/>).

## 1. Introduction

Large earthquakes often occur at the boundaries between oceanic and continental tectonic plates. In particular, the Japanese archipelago is surrounded by such plate boundaries. Consequently, highly accurate predictions of earthquake risk at such locations are necessary. At plate boundaries, the oceanic plate subducts beneath the continental plate, causing earthquakes as a result of friction between the plates, and sediments on the oceanic plate are scraped off and deposited onto the continental plate. This region is known as the accretionary prism where many large earthquakes that cause significant damage occur, such as the Tokai and Tonankai earthquakes. Therefore, the stress state and development mechanism of fault structures in the accretionary prism should be investigated to elucidate the scale and risk of future earthquakes. In addition, technology for accurately predicting the timing of large earthquakes by capturing the precursors of earthquakes should

be developed. Currently, *in situ* observational studies of stress and pore pressure in the accretionary prism [1] are being conducted, and seismic observation networks are being developed on the seafloor [2].

To date, general sandbox-scale experiments and simulations have been conducted on the dynamics of plate boundaries to investigate the formation process of the accretionary prism at the laboratory level; however, most of these experiments and simulations are limited to two-dimensional observations and analyses [3–5]. In particular, many studies have focused on the behavior of accretionary prism formation in the plate subduction direction, and effects of the fold and fault structures of the accretionary prism in the subduction direction on earthquakes have been investigated [6]. However, the accretionary prism exhibits different three-dimensional structures depending on the location, such as a wavy structure in the trench axis of the Nankai Trough or a linear structure off the coast of Chile. To understand the relationship between the accretionary prism structure and earthquakes, the conventional two-dimensional study design focusing only on the subduction direction is insufficient. However, the relationship between the accretionary prism structure along the trench axis and earthquake magnitude established to date has not been thoroughly investigated. To investigate the formation process of a three-dimensional accretionary prism structure, we conducted the world's largest discrete element method (DEM) simulation, which

\* Open Access for this article was sponsored by the Society of Powder Technology, Japan, through the KAKENHI Grant Number 18HP2009/ Grant-in-Aid for Publication of Scientific Research Results, Japan Society for the Promotion of Science, 2021.

<sup>†</sup> Japanese version published in JSPTJ, Vol.56 No.4 (2019); English version for APT received on Aug 17, 2021.

\* Corresponding author.

E-mail address: [nishiura@jamstec.go.jp](mailto:nishiura@jamstec.go.jp) (D. Nishiura).

is of the same scale as a 1 m<sup>2</sup> sandbox experiment (approximately 1.9 billion particles). We found that the arch-like stress chain structure developed inside the accretionary prism determined the three-dimensional rippled shape of the accretionary prism [7]. However, the existence of earthquake precursors and the relationship between the fault movement and the fluctuation observed on the undersea ground surface layer where the seismic observation network is established have not been clearly demonstrated. In addition, observations or analyses reported in the literature did not focus on small-scale fluctuations such as particle motion scales, and even when the indicators of earthquakes exist in the small-scale fluctuations observed using seismographs, they are regarded as measurement limits or noise.

In this study, we investigated the mechanical behavior of a sand bed with fault movement using a large-scale DEM simulation that can reproduce the accretionary prism formation process at the sandbox scale. We focused on the particle motion occurring before and after ground uplifting with fault formation. Furthermore, we measured the interior dynamics of the ground and fluctuations of particle motion in the ground surface layer. The aim is to carry out a detailed investigation of the possibility of monitoring the precursors of fault movement and to obtain useful information for future observations of submarine earthquakes.

## 2. Simulation methodology

### 2.1. Parallel computing algorithms for DEM

Although the basic DEM algorithm [8] was used in this study, hybrid parallelization was applied to achieve high-performance large-scale computing for real-scale granular particle simulations; this was applied with a message passing interface (MPI) library and an open multiprocessing (OpenMP) library. In particle simulation methods, such as the DEM, particles can migrate freely in space. Therefore, distributed-memory parallelization using static domain decomposition results in imbalance in the computational load of computational nodes. In this study, the dynamic load balancing method was used to dynamically change the computational domain to balance computational load among nodes [9]. To achieve shared-memory architectures, we used a highly efficient parallelization method that prevents concurrent write access to the same memory address by reordering the particle numbers [8,10]. Additionally, unlike other particle simulation methods, such as smoothed particle hydrodynamics and molecular dynamics, the DEM is more difficult to parallelize owing to tangential interactions between particles. Because the calculation of the tangential force requires the integrated amount of the relative displacement in the tangential direction between particles, parallelization must be performed to conserve information on the contacting particle pairs before and after updating the list of candidate contact pairs or changing the decomposed computational domain.

In dynamic load balancing, computational domain change and particle migration across computational nodes are performed when the list of candidate contact pairs is updated. Therefore, before changing the computational domain, the algorithm shown in Fig. 1 was used for preprocessing to conserve information on the contacting particle pairs. As a precondition, each particle must have both an independent particle number (as shown in Fig. 2(a)) and a serial number gInit\_p\_label for all nodes (as shown in Fig. 2(b)). Although this serial number does not change during computation, the particle number for each node changes owing to reordering and particle migration across computational nodes. First, the prefix sum of the number of candidate contact pairs, gPair for each particle, gIbox\_dom is calculated in each node. At this stage, each node possesses information on particles located in the domain, including up to only the sleeve region, which is shared with the

```

gIbox_(0)=0
!$OMP PARALLEL DO
DO i=1,gPnum_dom_ALL
    ii=gIbox_dom_all(i-1)
    DO j=gIbox_dom(i-1)+1,gIbox_dom(i)
        jj=gIbox_dom(j)
        if(i .eq. gJe(1,jj))then
            Init_j=gInit_p_label(gJe(2,jj))
            flag=1.0
        else
            Init_j=gInit_p_label (gJe (1,jj))
            flag=-1.0
        endif
        ii=ii+1
        gList(ii)=Init_j
        gPl(1,ii)=gPc(1,jj)*flag
        gPl(2,ii)=gPc(2,jj)*flag
        gPl(3,ii)=gPc(3,jj)*flag
        gPl(4,ii)=gUcnv(1,jj)*flag
        gPl(5,ii)=gUcnv(2,jj)*flag
        gPl(6,ii)=gUcnv(3,jj)*flag
    ENDDO
ENDDO
!$OMP END PARALLEL

```

Fig. 1. Preconditioning algorithm for inheriting particle pair information.

neighboring node, as shown in Fig. 3. Hence, by communicating with neighboring nodes, gPair for the particle in the sleeve region is accurately calculated. Subsequently, the prefix sum of gPair, gIbox\_dom\_all is re-calculated to obtain accurate information in the entire domain, including the sleeve region. Therefore, by calculating gIbox\_dom and gIbox\_dom\_all in advance, the algorithm shown in Fig. 1 can be evaluated in parallel on a shared memory within a node. Next, for each particle at each node shown in Fig. 3, pair information (tangential force gPc, normal vector gUcnv, and serial number of the other pair particle Init\_j) is stored in temporal arrays (gPl, gList) using the algorithm shown in Fig. 1. Because gPc and gUcnv are vector quantities, their signs must be considered in the data storing operation. As a prerequisite, gPc and gUcnv contain the interaction data from particle j to particle i under the condition that  $i < j$  based on Newton's third law. The pair particle numbers ( $i, j$ ) are stored in an array such as  $gJe(1,*) = i$  and  $gJe(2,*) = j$ , where \* is the candidate contact pair number. Therefore, because the interaction data is received by particle i from particle j if  $gJe(1,*)$  is  $i$ , the data can be stored in the temporal array without modification, as shown in the algorithm in Fig. 1. However, if  $gJe(1,*)$  is not  $i$ , the interaction data is received by particle j from particle i; then, it must be stored in opposite signs to become correct information from particle j to particle i.

Because of the preprocessing described above, the serial number of the other pair particle Init\_j is stored in gList, as shown in Fig. 4. The particle number  $i$  in the figure represents the unique number for each node shown in Fig. 2(a), and the particle number stored in gList is the common serial number gInit\_p\_label for all nodes shown in Fig. 2(b). While some elements of the array gList exist where no data was stored, these elements remain empty because the corresponding data is available in the

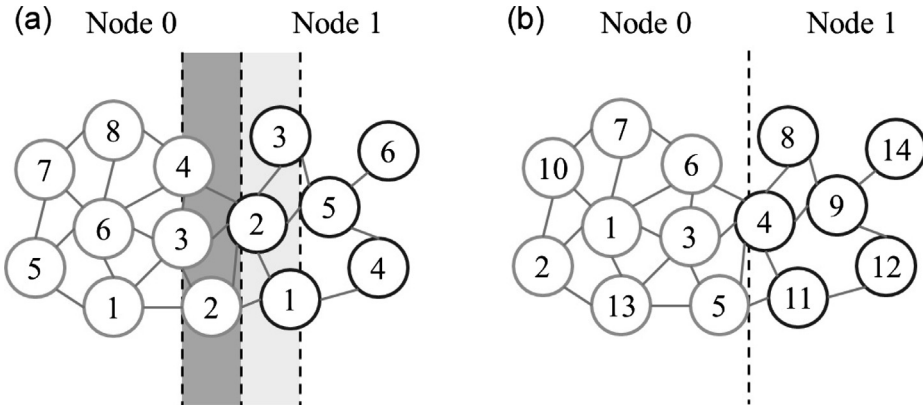


**Fig. 2.** Configuration of (a) independent particle number and (b) serial particle number in a neighbor computational domain.

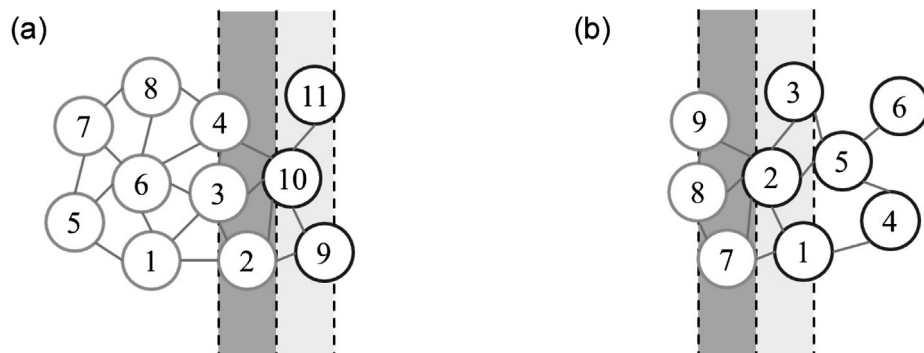


**Fig. 3.** Particle information in (a) Node 0 and (b) Node 1 as a neighbor computational domain.

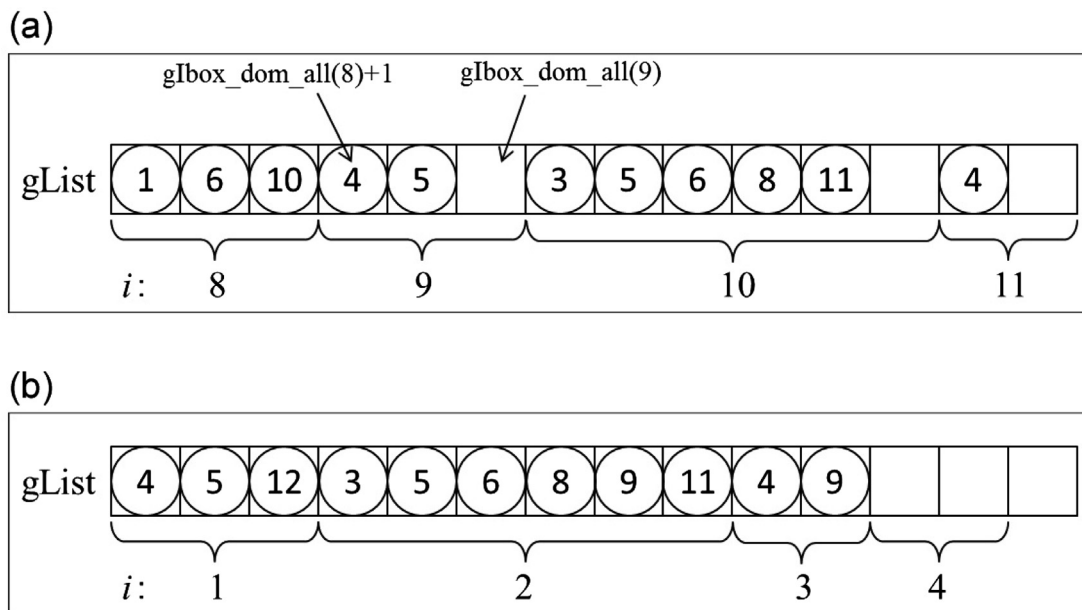


**Fig. 4.** Data structures of temporal array storing the pair information of particles located around a halo region in (a) Node 0 and (b) Node 1. The other pair particles are assigned a common serial number for all computational nodes.

neighboring nodes, and the data can be stored later through inter-node communication. For instance, the particle with  $i = 9$  in Node 0 is in the neighboring node, as shown in Fig. 3(a). Consequently, one piece of pair information is missing for the particle. As shown in Figs. 3(b) and 4(b), the missing element

is overwritten through inter-node communication using the corresponding information, that is pair information of Particle 1 in Node 1. By reserving the missing element on the array in advance, inter-node communication can be efficiently performed. As a result of the above preprocessing and inter-node communi-

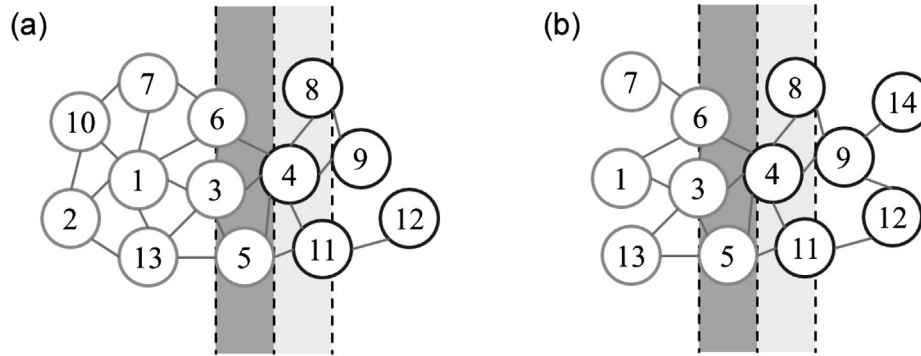


**Fig. 5.** Configuration of particle pairs obtained in (a) Node 0 and (b) Node 1 as a neighbor computational domain after the preconditioning process. Particles are assigned a common serial number for all computational nodes.

cation, correct pair information can be obtained for each particle in the computational domain, including the sleeve region, as shown in Fig. 5.

Next, we describe the method of inheriting pair information when the candidate contact pairs are updated or the computational domain is changed. In the proposed method, the boundary of the computational domain shifts only by the sleeve region when the computational domain is changed by a single dynamic load balancing process. Pair information (gPair, gList, and gPl) and particle information can be easily and accurately transferred because each node contains the correct pair information, including the sleeve region, owing to preprocessing as described above. However, in the proposed method, the particle numbers are sorted using the cell label to improve cache efficiency and the performance of shared-memory parallelization and inter-node communication. Therefore, the particle number must be consistent for the particles located in the shared boundary cells between computational nodes (halo region used for MPI communication) to ensure correct communication. In other words, depending on the types of sorting algorithms, the particle number can be assigned randomly for the particles located in the same cell, as shown in Fig. 6. Therefore, communicating only particle information will not lead to problems, such as positions and velocities. However, in communicating pair information, the particle that should inherit the pair information cannot be assigned. Therefore, in this study, the particle numbers were sorted in descending order of the serial particle number for the particles located in the same cell. This ensures the

consistency of the particle number in the entire computational domain. Another problem that arises if the particle number is inconsistent is that the order of calculation changes during the summation of the interparticle force for each particle, which causes the calculation results to differ based on the number of nodes as well as in each execution. However, the same calculation results can be obtained with or without parallelization by maintaining consistency in the particle number, as shown in Fig. 7.

Finally, we describe the method of transferring the pair information stored in the temporal array. After updating a new candidate contact pair, the algorithm shown in Fig. 8 is used to verify whether the pair remains a pair before the update. The current pair particle number is stored in the array of gle, and the serial numbers of the past other pair particles are stored in the array of gList. Therefore, the serial number Init\_j corresponding to the current other pair particle number gle(2,\*) is searched to determine its inclusion in the array of gList. Inclusion indicates that the current pair is also a pair in the past. At this point, if the prefix sum of the number of past pairs, glbox, is used for the search area in gList, then it is sufficient to search the array index range from glbox(i-1)+1 to glbox(i) for particle i. Subsequently, if the pair is also a pair in the past, then the interaction data is transferred from the temporal array gPl for that pair to the array of tangential forces gPc and normal vectors gUcnv.

By applying the above method, the pair information necessary for tangential force calculation in the parallelized DEM can be inherited. In terms of the computational performance of the simu-

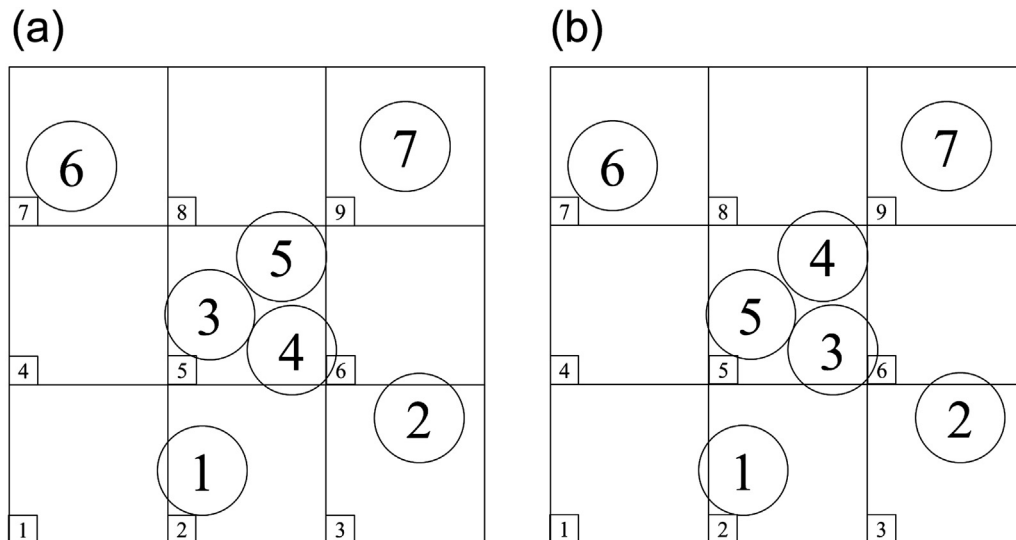


**Fig. 6.** (a) and (b) possible states for particle number sorted by cell label.

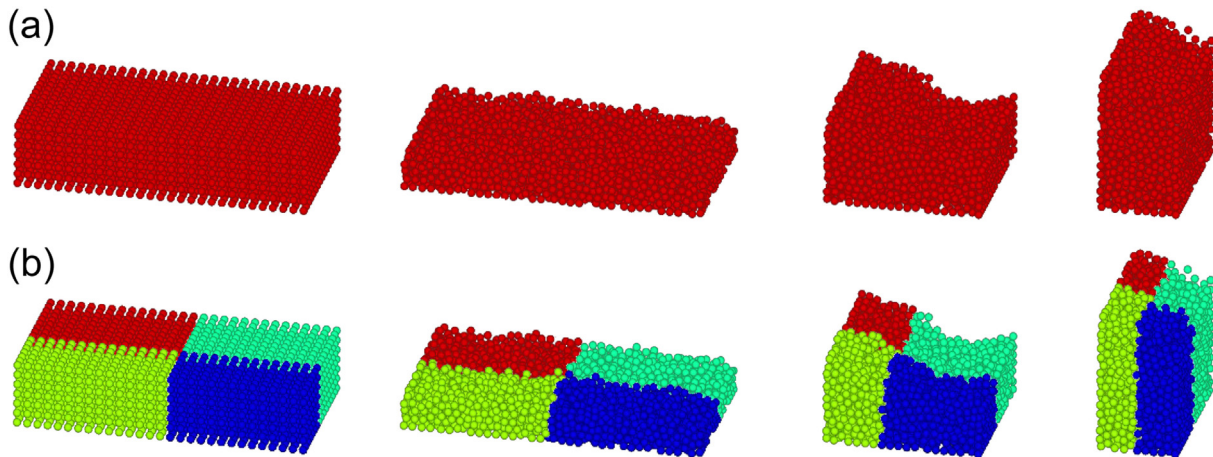


**Fig. 7.** Comparison of particle motion obtained by computing (a) without and (b) with distributed-memory parallelization. The same colored particles represent particles located on the same computational node.

```

!$OMP PARALLEL DO
DO jik=1,gNje
  gPc(1,jik)=0.d0
  gPc(2,jik)=0.d0
  gPc(3,jik)=0.d0
  gUcnv(1,jik)=0.d0
  gUcnv(2,jik)=0.d0
  gUcnv(3,jik)=0.d0
  i=gJe(1,jik)
  j=gJe(2,jik)
  Init_j=gInit_p_label(j)
  DO ii=gIbbox(i-1)+1,gIbbox(i)
    IF(gList(ii) .eq. Init_j)THEN
      gPc(1,jik)=gPl(1,ii)
      gPc(2,jik)=gPl(2,ii)
      gPc(3,jik)=gPl(3,ii)
      gUcnv(1,jik)=gPl(4,ii)
      gUcnv(2,jik)=gPl(5,ii)
      gUcnv(3,jik)=gPl(6,ii)
    EXIT
  ENDIF
ENDDO
ENDDO
!$OMP END PARALLEL

```

**Fig. 8.** Algorithm for inheriting particle pair information when the candidate contact pairs are updated or the computational domain is changed.

lation using this dynamic load balancing method, the computational speed obtained using 2.4 billion particles in the computational domain presented in Section 2.2 was 3.47 times

faster, the parallelization efficiency was 88.7%, and the effective parallelization ratio was 99.99341% when the number of computational nodes was increased from 512 to 1936 (3.78 times) using the Earth Simulator. Furthermore, using a K computer under the same conditions, when the number of computational nodes was increased from 1024 to 16384, the parallelization efficiency was 96.0%, and the effective parallelization ratio was 99.99787% [11]. These results show that the parallelization performance is still high as the number of nodes increased.

## 2.2. Computational conditions

In this study, spherical particles with an average diameter of 227.5  $\mu\text{m}$ , which are equivalent to the actual particles of Toyoura sand, were uniformly spread with a layer thickness of 18.8 mm in a 1  $\text{m}^2$  sandbox, as shown in Fig. 9. The particle size distribution remained uniform within  $\pm 22.5 \mu\text{m}$  from the mean particle size, considering the computational load. Furthermore, a high-density sand layer was created by allowing frictionless particles to descend freely using gravity. In the case of random particle placement using random numbers in distributed memory parallelization with domain decomposition, if the same random number was used in computation nodes, the particle placements will also be the same and will lose randomness. Hence, different sets of random numbers were used at each computation node. The number of particles was approximately 1.9 billion under the above conditions. After completing the initial placement, the coefficients of interparticle friction and rolling friction were set to reproduce the fault angle obtained from the experiment, and the walls of the sandbox, other than the back stop side, were moved at a constant speed in the direction of shortening the sand bed (positive in the x-direction) to form an accretionary prism in the sandbox. The wall movement speed was set to 0.1 m/s based on the computational time. The friction on both side walls was set to zero to reduce the wall effect. In this study, we simulated the accretionary prism formation process for 5 s in real time using 4000 nodes of the K computer or 2000 nodes of the Earth Simulator for 24 h. Additionally, a case where the particle size was doubled was simulated to verify the effect of particle size. The other computational conditions applied are presented in Table 1. The Young's modulus was set to be smaller than that of the actual Toyoura sand to limit the computation time within 24 h to account for the computational load (discrete time). Because the coefficient of restitution and Poisson's ratio are difficult to measure and did not significantly affect the shape of the

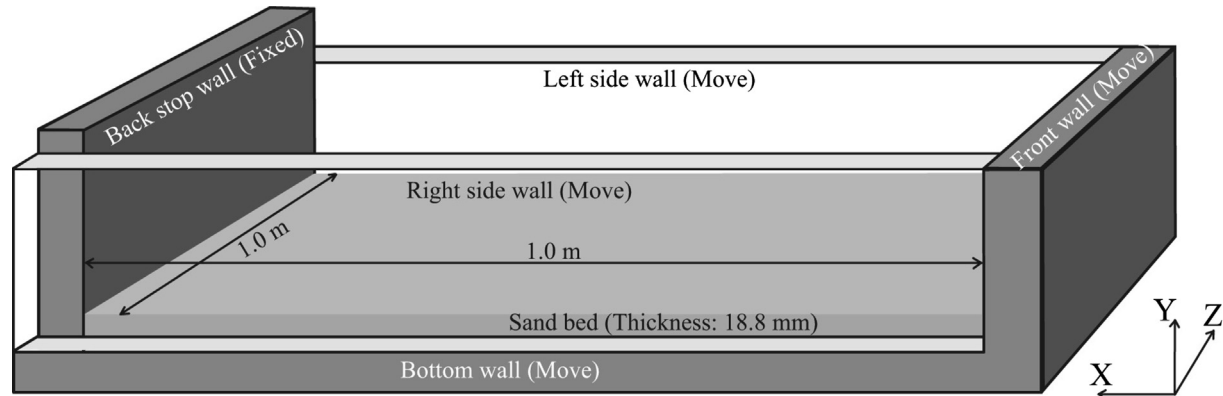


**Fig. 9.** Overview of sandbox used in analog and numerical experiments.

**Table 1**  
Particle properties used in the DEM simulation.

Parameters	Values	Unit
Particle diameter	$227.5 \pm 22.5$	[μm]
Particle density	2,600	[kg/m <sup>3</sup> ]
Young's modulus	0.01	[GPa]
Poisson ratio	0.2	[–]
Coefficient of friction (particle-particle)	0.6	[–]
Coefficient of friction (particle-wall)	0.25	[–]
Coefficient of restriction	0.2	[–]
Coefficient of rolling friction	0.05	[–]

fault or the stress state in the sand bed, plausible values were set empirically to avoid unstable computations.

### 3. Results and discussion

#### 3.1. Sand bed surface

The fault structures visible from the surface and side of the sand bed are shown in Fig. 10. The experimental and simulation results

obtained by doubling the particle size are also shown for comparison. In the simulations, the particle layers were initially colored to resemble stripes in the height direction to enhance the visualization of the fault structure. By moving the wall, the particle layer is compressed; when the Mohr-Coulomb failure criterion is exceeded, faults (back thrust and fore thrust) are generated in a V-shape and the particle layer is uplifted. The uplift of the sand bed surface layer, the wavy structure in the depth direction (trench axis direction), and particles gathering in the valley just above the fault to form a small hill, which were observed experimentally, were reproduced in the simulation. In contrast, when the particle size was increased two-fold, the sharpness of the fault plane diminished slightly in the simulation; nonetheless, the results were similar to those of a real particle size. The simulation results obtained under the two-fold particle size condition, considering the ease of analysis and limited computational resources, were analyzed and a detailed discussion is presented in this paper.

The force that the wall of the sandbox receives from the particle bed is illustrated in Fig. 11 to clarify the relationship between fault movement and particle bed pressure. As the wall is moved, the particle bed is compressed and the force acting on the back stop wall increases gradually. Subsequently, when a fault occurs in the particle bed, the stress is abruptly released and the force acting on the

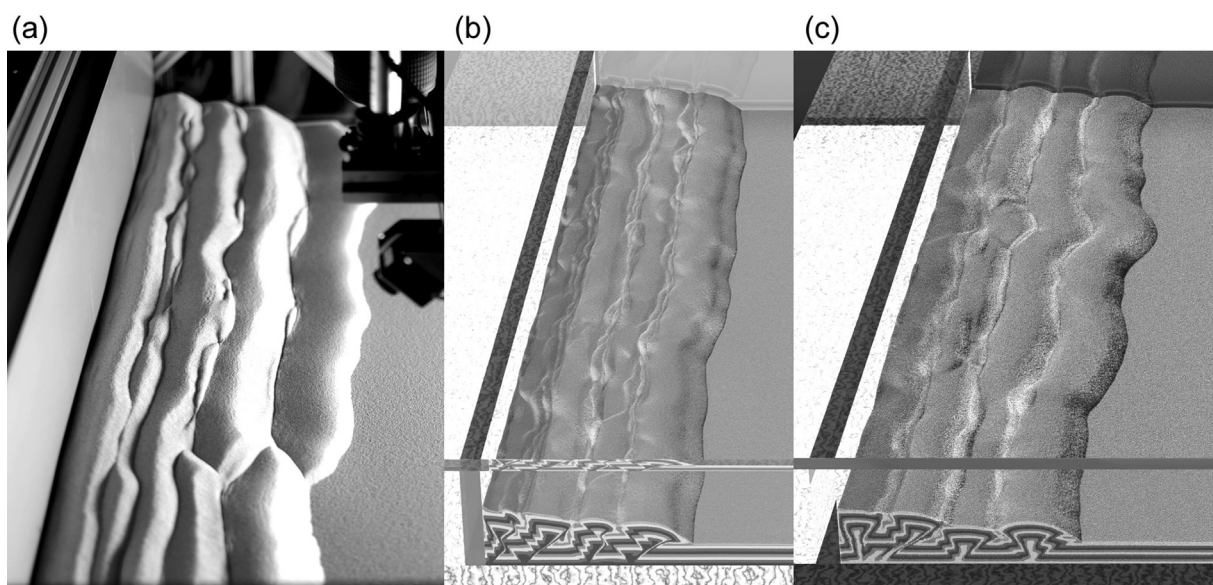


**Fig. 10.** Snapshots of accretionary prisms obtained by (a) analog experiment and DEM simulations using (b) 1.9 and (c) 0.24 billion particles in the sandbox. Average particle diameter of (b) is 227.5 mm, which is almost the same as that of (a) analog experiment and is half the size of (c).

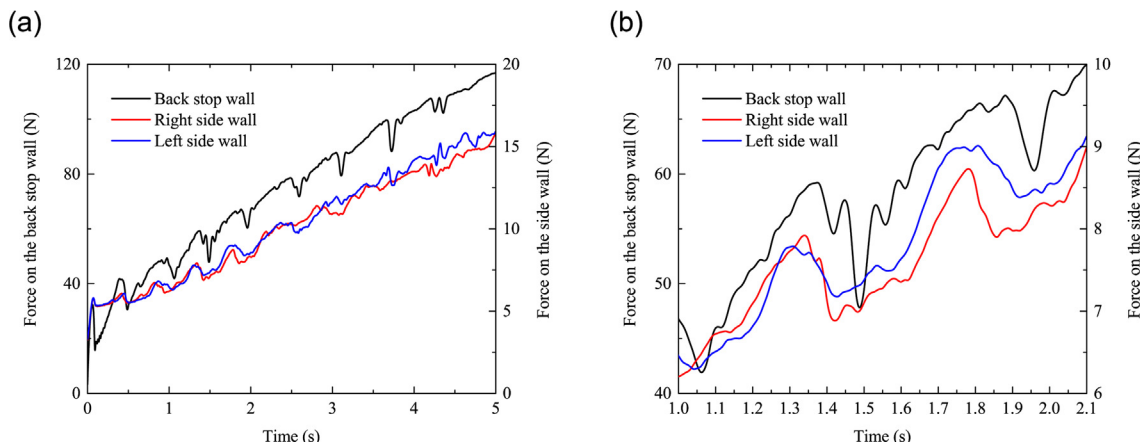


**Fig. 11.** (a) Overview and (b) close-up view of time evolution of force acting on the walls of the sandbox.

wall decreases. The same tendency was observed for the right and left side walls. However, the decrease in the force started slightly earlier on the side walls than on the back stop wall, as shown in Fig. 11(b). The reason for this behavior will be discussed in Section 3.2. However, it is speculated that the fault begins to form near the side wall and gradually develops into a single connected fault.

Moreover, the particle behavior of the ground surface layer during the period shown in Fig. 11(b), which represents the new fault motion occurring at approximately 1.5 and 2.0 s, was analyzed comprehensively to further investigate the relationship between the fault motion and the fluctuation observed in the ground surface layer. Fig. 12 shows the acceleration of a single particle located at coordinates (0.55 m, 0.0188 m, 0.45 m) when the position of the front wall is considered as the origin of the x-axis. This particle was located slightly in front (front wall side) of the uplift with fault movement. Because the side wall force in this case began to decrease at 1.35 s and 1.8 s as shown in Fig. 11(b), the new fault movement was assumed to have started at these times. However, before the start of the fault movement (shaded area in the figure), the particles in the ground surface layer started fluctuating, as shown in Fig. 12. In particular, although the fluctuation in the x-axis direction was significant, fluctuations were also observed in the y- and z-axial directions, which are orthogonal to the shortening direction of the ground, prior to the initiation of fault motion.

This suggests that fault movement in the sandbox can possibly be predicted in advance by observing the microscopic particle movement in the ground surface layer.

### 3.2. Sand bed interior

In the preceding section, we captured the micro-fluctuation of particles in the ground surface layer before the initiation of fault movement. Next, to elucidate why the particle motion can be indicative of the initiation of fault motion, we performed a detailed investigation of the effect of motion inside the ground on fluctuations of the ground surface layer. The spatial distribution of particle displacements in the y-axis (vertical direction) of the horizontal cross section at a height of 7.5 mm for the fault motion occurring between 1.6 s and 2.0 s is shown in Fig. 13. The cross section was partitioned into grids with a spatial resolution of 5 mm, and the spatial distribution of particle displacement was obtained by averaging in each grid. In each figure, the left and right ends represent the back stop and front walls, respectively. The figures show the instantaneous displacement distribution observed in a time window of 0.01 s. At 1.6 s, the moving fault stopped gradually, and a new fault formation was initiated in the front (front wall side) near both side walls; at 2.0 s, the faults connected to a single fault and moved in unison. It can be observed from this result that the force applied to both side walls started to decrease before a force was applied to the back stop wall as shown in Fig. 11(b). Although the fault was formed from the side wall under these computational conditions, it was confirmed that the location of the fault initiation changed when the observation time and the initial placement of the particles were changed. Additionally, although the previously active fault started to move again simultaneously at the back of the current active fault (near the back stop wall), it was confirmed that the re-activated fault movement subsided at 2.0 s. This indicates that the formation of the new fault began approximately 0.1 s earlier than the time ( $t = 1.8$  s) when the wall force started to decrease, as shown in Fig. 11(b). However, particle fluctuation started before 1.7 s as shown in Fig. 12, suggesting that some ground motion occurred before the initiation of fault motion, resulting in the fluctuation of particles on the ground surface.

Next, the spatial distribution of the contact force between particles in the x-axis direction in the same horizontal section as that shown in Fig. 13 was investigated to clarify the reason for particle fluctuation. The results are shown in Fig. 14. The spatial distribution of the interparticle contact force was obtained by averaging the values of the x-axis direction components of the contact force (sum of normal and tangential forces) per par-

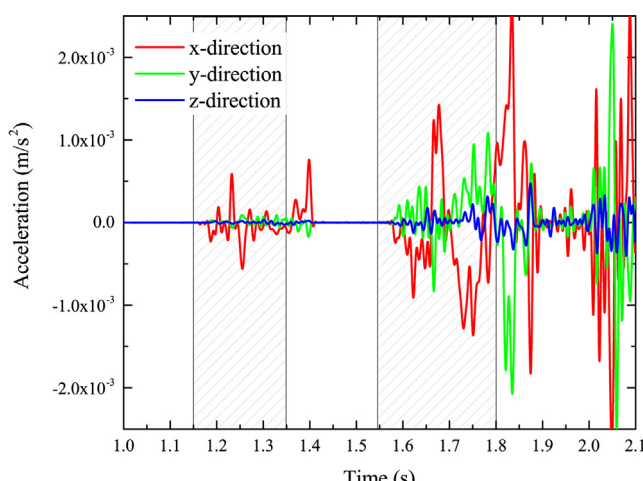


**Fig. 12.** Acceleration of a particle located on the surface of the sand bed.

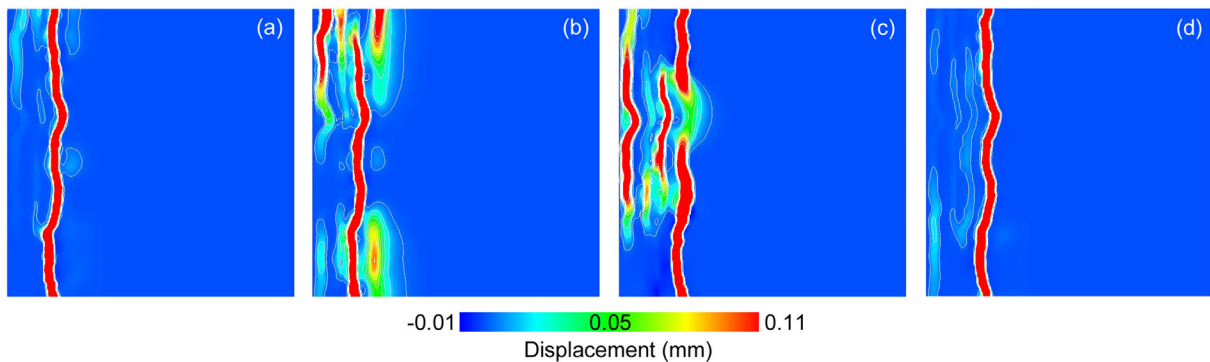


**Fig. 13.** Spatial distributions of particle displacement in the horizontal cross-section of the sand bed at (a) 1.6 s, (b) 1.7 s, (c) 1.85 s, and (d) 2.0 s between the initiation of a new thrust generation and its termination.

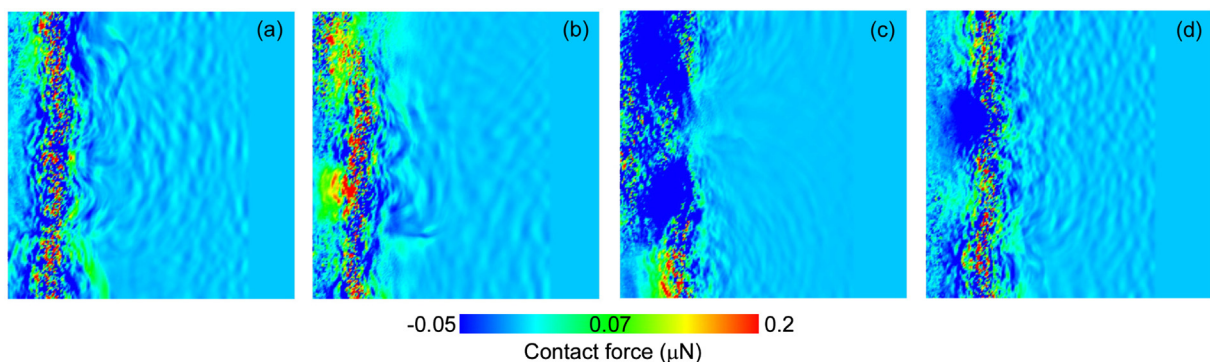


**Fig. 14.** Spatial distribution of particle contact force in the horizontal cross-section of the sand bed at (a) 1.6 s, (b) 1.7 s, (c) 1.85 s, and (d) 2.0 s between the initiation of a new thrust generation and its termination.

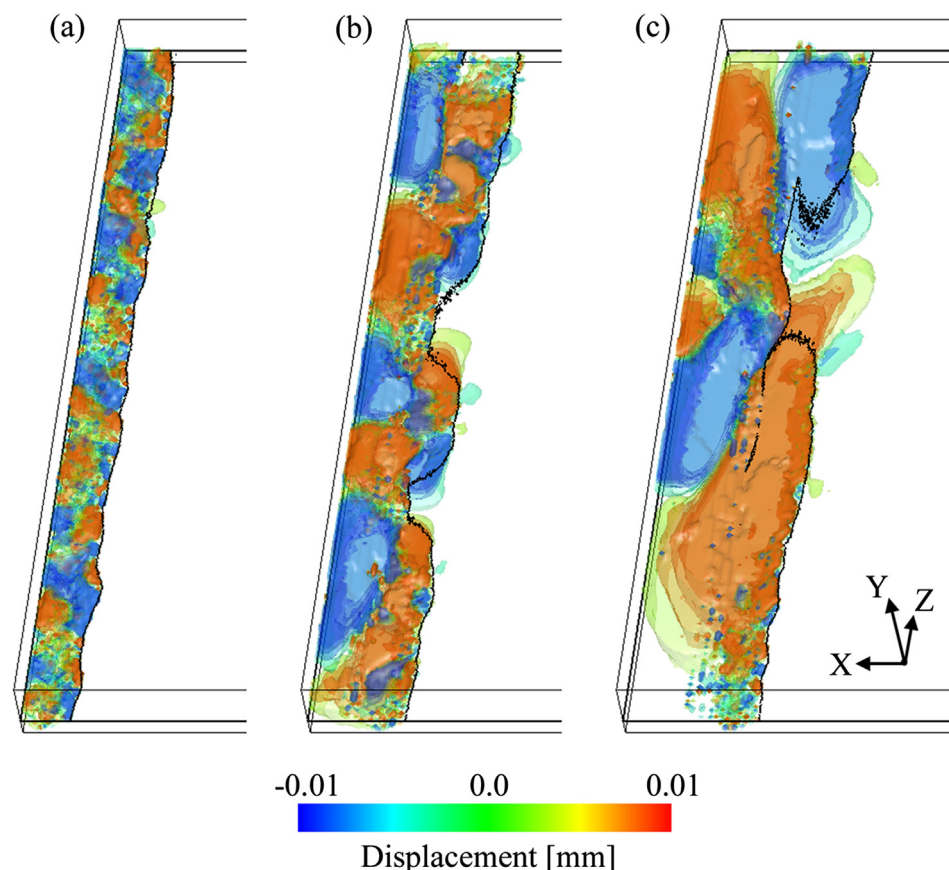


**Fig. 15.** Three-dimensional spatial distribution of particle displacement in the z-direction at the time of (a) first, (b) second, and (c) third faulting events.

ticle in each grid. At 1.6 s, the fluctuation of the interparticle contact force generated by the sliding motion of the fault propagated like a wave in the particle bed. Subsequently, at 1.85 s, the fluctuation and propagation of the interparticle force were confirmed to be insignificant in the region where the faults had not yet started to move because the newly formed faults near both side walls had not yet completely connected to a single fault, as shown in Fig. 13. At 2.0 s, fault formation was completed, and the newly formed faults resulted in strong interparticle force propagation. It is speculated that propagation of the interparticle force affected the fluctuation of particle motion on the ground surface. Particle fluctuation stopped abruptly between 1.85 s and 2.0 s as shown in Fig. 12, which coincides with the period of temporary reduction of the fluctuation of interparticle force as shown in Fig. 14. The interparticle force subsequently fluctuated owing to the motion of the newly formed fault, and the particles fluctuated simultaneously on the ground surface. Hence, the particle fluctuations identified before 1.7 s, previously considered to be a precursor to the initiation of fault formation, could be due to fluctuations of the interparticle force generated by the previous fault movement. Meanwhile, it was also observed that a period of reduced interparticle force or particle fluctuation occurred when a new fault began to form. Therefore, the reduction in particle fluctuation from 1.4 s to 1.6 s shown in Fig. 12 possibly indicates the formation of a new fault.

Finally, the vertical component of the ground motion is shown in Fig. 13, whereas the horizontal component (z-direction), which is perpendicular to the shortening direction of the ground (x-direction), exhibits characteristic motions and is described herein. Fig. 15 shows the three-dimensional spatial distribution of the instantaneous particle displacement in the z-direction observed in a time window of 0.01 s when the first, second, and third faults were forming and beginning to move. When the first fault was formed, the particles exhibit a relatively small collective motion and the motion direction alternated in the opposite direction of the side wall. As the second and third faults formed subsequently, the particles developed into a larger collective motion. It was observed that the particles propagated collectively in the z-direction even though the wall was moving in the x-direction. Therefore, the force on the side wall increased with the particle motion in the z-direction, and then decreased when the fault was formed as shown in Fig. 11. In other words, compressive stresses acted on the sand bed in both the x- and z-directions, and the fault exhibited a complex three-dimensional shape owing to the bidirectional compression. In addition, a microscopic observation was performed at the particle level by visualizing the stress chains to clarify the factors that caused the evolution in the collective motion of particles in the horizontal direction and the increase in the force applied to the side walls [12]. Fig. 16 shows the visualization of the stress chains in the horizontal section of the sand bed.

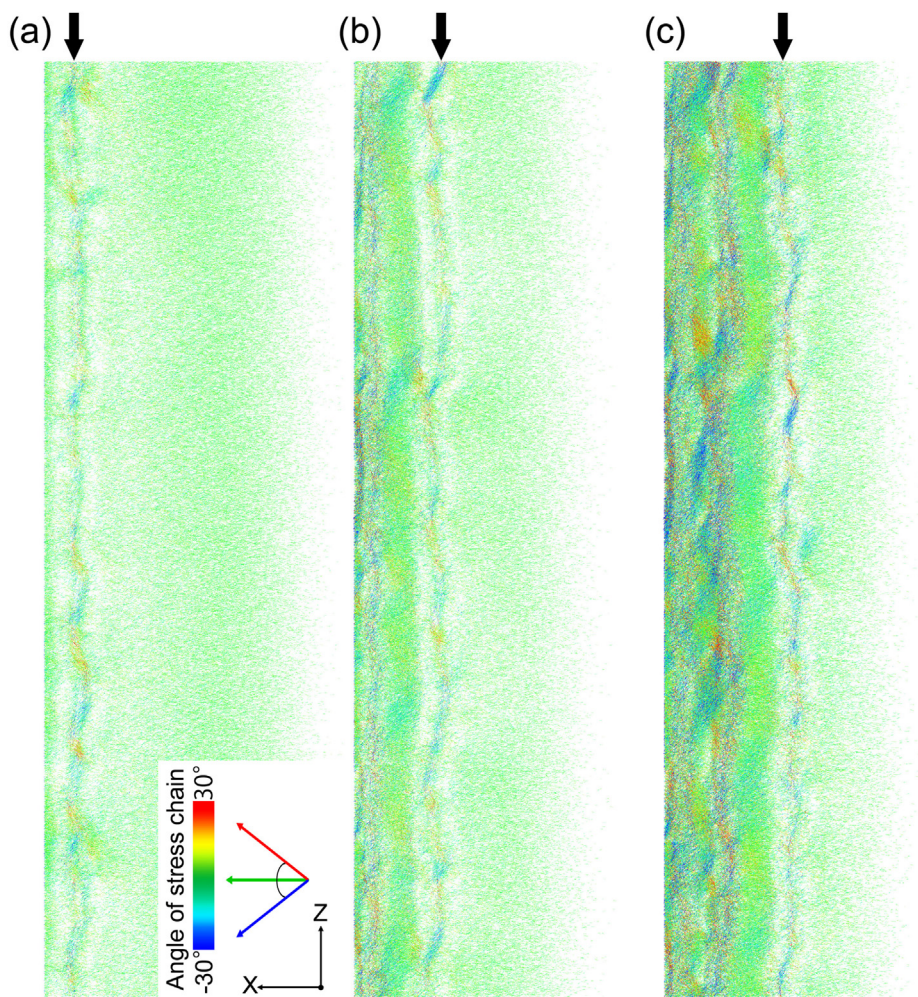


**Fig. 16.** Spatial distribution of stress chains developed among contacting particles in the horizontal cross-section of the sand bed at the time of (a) first, (b) second, and (c) third faulting events.

The arrows at the top of each figure indicate the location of the newly formed fault, and the stress chains at this location were developed in the uplifted surface layer between the back thrust and fore thrust. The stress chains are connected in the z-direction, and it is considered that this allows the force to be transferred to the side wall and develop the collective motion of the particles. Furthermore, a previous study demonstrated that the structure of the connected stress chains determines the rippled fault shape [7]. It should be noted that the width of the sandbox was sufficiently wide such that the effect of the side walls on the simulation results is negligible. In addition, simulations were performed with periodic boundary conditions in the direction of the side walls, and it was confirmed that the effect of the side walls is negligible for particle collective motion and stress chain formation in the z-direction under these computational conditions.

#### 4. Conclusion

We developed the world's largest-scale DEM simulation code and analyzed the mechanical behavior of ground with fault motion at a scale of 1 m<sup>2</sup> sandbox to obtain useful information regarding future submarine earthquake observations.

We found that a period of reduced particle fluctuation in the ground surface layer occurred prior to the initiation of a new fault movement. Fluctuation of the interparticle contact force caused by fault movement in the ground, which decreased until the new fault was completely formed and starts moving, significantly affected the particle fluctuation observed in the ground surface layer. This could suggest that long-term observation of microscopic particle motion in the ground surface layer can facilitate the prediction of fault motion occurring in the sandbox in advance.

In addition, it was discovered that the fault shape was spontaneously rippled because of microscopic disturbances at the particle scale (random particle arrangement, particle size distribution, spatial distribution of particle packing ratio, etc.) even when the sand bed was macroscopically homogeneous in the initial state. In particular, stress chains developed in the horizontal direction perpendicular to the shortening direction of the ground, and stress was transferred considerably in the direction of the side wall, accompanied by the collective motion of particles against the side wall. The scale of this collective motion increased as new faults were formed, and the fault structure became more complex in three dimensions.

In this study, we demonstrated the possibility of precursory observation of fault motion based on a real-scale DEM simulation of sandbox experiments. Furthermore, we clarified that the fault shape is caused by the initial disturbance in the ground at the particle scale, and it developed with collective particle motion due to the connection of stress chains, which was rippled spontaneously thereafter. To apply the results obtained at the sandbox scale to practical applications in the future, their relationship with actual phenomena observed on the seafloor must be thoroughly analyzed.

#### Declaration of Competing Interest

The authors declare that they have no known competing financial interests or personal relationships that could have appeared to influence the work reported in this paper.

#### Acknowledgements

The sandbox simulations were performed on the Earth Simulator at the Japan Agency for Marine-Earth Science and Technology (JAMSTEC) and K computer at RIKEN. This study was supported by the Earth Simulator project of JAMSTEC (Project name: Development of Advanced Simulation Methods for Solid Earth Simulations) and Post-K project of Ministry of Education, Culture, Sports, Science and Technology (Project ID: hp160221). Open Access for this article was sponsored by the Society of Powder Technology, Japan, through JSPS KAKENHI Grant Number 18HP2009, Grant-in-Aid for Publication of Scientific Research Results, Japan Society for the Promotion of Science, 2021.

#### References

- [1] W. Lin, T.B. Byrne, M. Kinoshita, L.C. McNeill, C. Chang, J.C. Lewis, Y. Yamamoto, D.M. Saffer, J.C. Moore, H.-Y. Wu, T. Tsuji, Y. Yamada, M. Conin, S. Saito, T. Ito, H. J. Tobin, G. Kimura, K. Kanagawa, J. Ashi, M.B. Underwood, T. Kanamatsu, Distribution of stress state in the Nankai subduction zone, southwest Japan and a comparison with Japan Trench, *Tectonophysics* 692 (2016) 120–130.
- [2] K. Kawaguchi, S. Kaneko, T. Nishida, T. Komine, Construction of the DONET real-time seafloor observatory for earthquakes and tsunami monitoring, in: *SEAFLOOR OBSERVATORIES*, Springer Praxis Books, Springer, Berlin, Heidelberg, 2015, pp. 211–228.
- [3] T. Dotare, Y. Yamada, J. Adam, T. Hori, H. Sakaguchi, Initiation of a thrust fault revealed by analog experiments, *Tectonophysics* 684 (2016) 148–156.
- [4] Y. Yamada, K. Baba, A. Miyakawa, T. Matsuoka, Granular experiments of thrust wedges: insights relevant to methane hydrate exploration at the Nankai accretionary prism, *Mar. Pet. Geol.* 51 (2014) 34–48.
- [5] T. Hori, H. Sakaguchi, Mechanism of décollement formation in subduction zones, *Geophys. J. Int.* 187 (2011) 1089–1100.
- [6] Y. Ogawa, Various perspectives on accretionary wedge formation and related phenomena, *J. Geogr.* 119 (2010) 153–172.
- [7] M. Furuichi, D. Nishiura, O. Kuwano, A. Bauville, T. Hori, H. Sakaguchi, Arcuate stress state in accretionary prisms from real-scale numerical sandbox experiments, *Sci. Rep.* 8 (2018) 8685.
- [8] D. Nishiura, H. Sakaguchi, Parallel-vector algorithms for particle simulations on shared-memory multiprocessors, *J. Comput. Phys.* 230 (2011) 1923–1938.
- [9] M. Furuichi, D. Nishiura, Iterative load-balancing method with multigrid level relaxation for particle simulation with short-range interactions, *Comput. Phys. Commun.* 219 (2017) 135–148.
- [10] D. Nishiura, M. Furuichi, H. Sakaguchi, Computational performance of a smoothed particle hydrodynamics simulation for shared-memory parallel computing, *Comput. Phys. Commun.* 194 (2015) 18–32.
- [11] M. Furuichi, D. Nishiura, M. Asai, T. Hori, The first real-scale DEM simulation of a sand-box experiment using 2.4 billion particles, in: Proc. SC17. The International Conference for High Performance Computing, Networking, Storage and Analysis, Denver, CO, United States, 2017, P21, available at [https://sc17.supercomputing.org/SC17%20Archive/tech\\_poster/tech\\_poster\\_pages/post113.html](https://sc17.supercomputing.org/SC17%20Archive/tech_poster/tech_poster_pages/post113.html) (accessed on August 1st, 2021).
- [12] J.F. Peters, M. Muthuswamy, J. Wibowo, A. Tordesillas, Characterization of force chains in granular material, *Phys. Rev. E* 72 (2005) 041307.